Supporting Information for

DFT-guided crystal structure re-determination and lattice dynamics of the intermetallic actinoid compound UIr

Malte Sachs[a], Sergei I. Ivlev[b], Martin Etter[b], Matthias Conrad[a], Antti J. Karttunen[c] and Florian Kraus[a]*

[a] *Fachbereich Chemie, Philipps-Universität Marburg, Hans-Meerwein-Straße 4, 35032 Marburg, Germany*

[b] *Deutsches Elektronen-Synchrotron (DESY), Notkestraße 85, 22607 Hamburg*

[c] *Department of Chemistry and Materials Science, Aalto University, Kemistintie 1 FI-02150 Espoo, Finland*

Corresponding author address:
Name: Florian Kraus
Philipps-Universität Marburg, Fachbereich Chemie
Hans-Meerwein-Straße 4, 35032 Marburg, Germany
Mail: f.kraus@.uni-marburg.de
Telefon: +49 6421 28 – 26 66 8

S1 Supporting information to section 2: Experimental part

S1.1 Crystal structure redetermination

Table S 1: Selected single crystal crystallographic data and details of the structure determination of UIr.

Formula	UIr
Molar mass / g·mol^{-1}	430.25
Space group (No.)	$P2_1/c$ (14)
Pearson symbol	$mP16$
[a] a / Å	5.6119(6)
[a] b / Å	10.5862(7)
[a] c / Å	5.5908(7)
[a] β / °	98.944(7)
V / Å^3	328.10(6)
Z	8
$\rho_{calc.}$ / g·cm^{-3}	17.42
μ / mm^{-1}	178.97
Color	metallic grey
Crystal morphology	wedge
Crystal size / mm^3	0.071 · 0.050 · 0.045
T / K	293
λ / Å	0.71073 (Mo- $K_{\bar{\alpha}}$)
No. of reflections	13815
θ range / °	3.676, 34.937
Range of Miller indices	$-8 \le h \le 8$
	$-16 \le k \le 17$
	$-8 \le l \le 8$
Absorption correction	Numerical (X-Shape, X-Red32)
T_{min}, T_{max}	0.0049, 0.0485
R_{int}, R_σ	0.127, 0.057
Completeness of the data set	0.99
No. of unique reflections	1444
No. of parameters	30
No. of restraints	0
No. of constraints	8
S (all data)	1.139
$R(F)$ ($I \ge 2\sigma(I)$, all data)	0.044, 0.062
$wR(F^2)$ ($I \ge 2\sigma(I)$, all data)	0.109, 0.126
Twin ratio	0.481(3)
$\Delta\rho_{max}$, $\Delta\rho_{min}$ / e·Å^{-3}	6.77, −6.83

[a] The cell parameters are from the powder X-ray diffraction experiment.

Table S 2: Selected crystallographic data and details of the Rietveld refinement of UIr.

Formula	UIr
Molar mass / g·mol^{-1}	430.25
Space group (No.)	$P2_1/c$ (14)
Pearson symbol	$mP16$
a / Å	5.6119(6)
b / Å	10.5862(7)
c / Å	5.5908(7)
β / °	98.944(7)
V / Å^3	328.10(6)
Z	8
$\rho_{calc.}$ / g·cm^{-3}	17.42
Color of the powder	metallic-grey
T / K	298
λ / Å	0.20709 (Synchrotron)
$2\theta_{min}$, $2\theta_{max}$, $2\theta_{step}$ / °	0.006, 13.285, 0.003
No. of data points	5000
No. of parameters	44
No. of restraints	0
No. of constraints	8
Peak shape function	Pseudo-Voigt
Anisotropic particle broadening	Spherical harmonics up to 4th order
Anisotropic strain broadening	Tensor method by Stephens and coworkers
Background	Legendre polynomial of 14th order
S	3.67
R_p, R_{wp} *	0.049, 0.058
$R_B(I)$	0.029
$\Delta\rho_{max}$, $\Delta\rho_{min}$ / e·Å^{-3}	1.75, −1.71

* Background-corrected R-factors

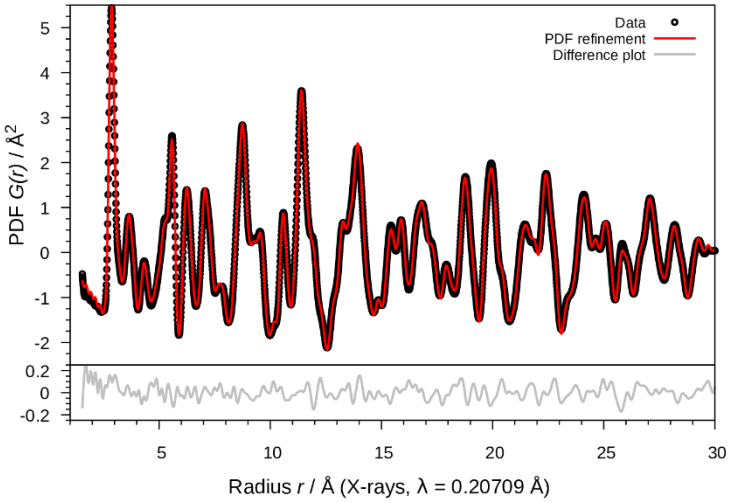

Figure S 1: PDF plot and refinement of UIr at 298 K in space group $P2_1$: experimentally obtained PDF (blue), calculated PDF (red), and difference curve (grey). *R* factors: R_p = 5.9 %, wR_p = 5.8 %.

Table S 3: Atomic positions and isotropic displacement parameters of UIr in comparison with literature data. All atoms occupy the position 2*a* and the site symmetry 1. The atomic coordinates of our model were transformed with respect to the conventional unit cell setting of the space group $P2_1$ with the transformation matrix $\boldsymbol{T}$ given below. The atoms U1 and $U1_1$ and the other corresponding atomic pairs occupy the same 4*e* site in the $P2_1/c$ setting..

Atom	*x*		*y*		*z*		U_{eq} / pm²	
	This work	Lit	This work	Lit	This work	Lit	This work	Lit
U1	0.5998(2)	0.6024(8)	0.04699(8)	0.044(1)	0.1389(2)	0.154(1)	90(2)	38(1)
$U1_1$	0.0998	0.123(2)	0.26461	0.264300	0.1389	0.107(2)	90	165(3)
U2	0.1560(2)	0.1484(8)	0.04388(8)	0.0462(8)	0.6091(2)	0.6008(6)	99(2)	38(1)
$U2_1$	0.3440	0.381(2)	0.7677	0.768(2)	0.3909	0.347(3)	99	190(3)
Ir1	0.5948(2)	0.633(1)	0.3112(1)	0.3107(8)	0.0999(2)	0.1508(8)	101(2)	279(3)
$Ir1_1$	0.0948	0.0955(8)	0.0004	0.0000(9)	0.0999	0.0935(9)	101	38(1)
Ir2	0.1607(2)	0.116(1)	0.3098(1)	0.310(1)	0.6493(2)	0.6065(9)	104(2)	279(3)
$Ir2_1$	0.3393	0.3445(8)	0.5018	0.502(1)	0.3507	0.3391(9)	104	51(2)

The transformation matrix $\boldsymbol{T} = \begin{pmatrix} \mathbf{0} & \mathbf{0} & \mathbf{1} & \mathbf{0} \\ \mathbf{0} & \mathbf{-1} & \mathbf{0} & \mathbf{-0.0942} \\ \mathbf{1} & \mathbf{0} & \mathbf{0} & \mathbf{1/4} \end{pmatrix}$.

Group-subgroup relation of the CrB type and the PdBi type

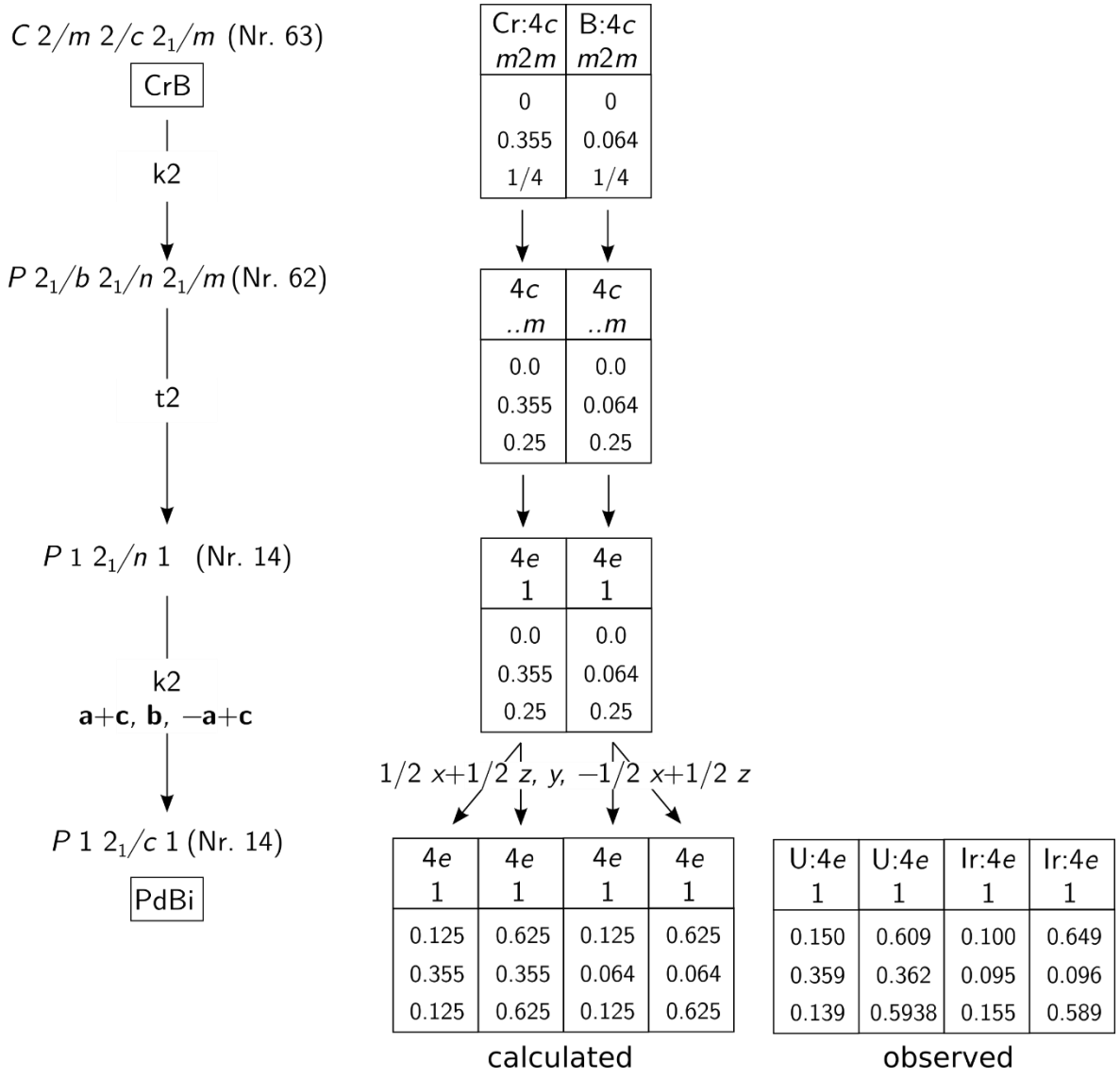

Figure S 2: Group-subgroup relationship of the CrB (*Cmcm*, *oS*8) and the PdBi ($P2_1/c$, *mP*16) structure type.

Table S 4: Selected interatomic distances *d* for UIr in comparison to literature and spin-polarized DFT calculations at 0 K. The multiplicity is always one. The atomic coordinates are given with respect to the conventional unit cell setting of the subgroup $P2_1$ of UIr. The atoms U1 and $U1_1$ and the corresponding other atomic pairs occupy the same 4*e* site in the $P2_1/c$ setting.

Atom 1	Atom 2	*d* / Å		
		Literature	This work	DFT
U1	Ir1	2.82(1)	2.805(2)	2.7924
	$Ir2_1$	2.84(2)	2.861(2)	2.8482
	$Ir1_1$	2.85(2)	2.841(2)	2.8269
	$Ir2_1$	2.85(2)	2.872(2)	2.8637
	$Ir1_1$	2.87(2)	2.853(2)	2.8455
	Ir2	3.12(2)	3.003(2)	3.0618
	Ir1	3.17(1)	2.959(2)	2.9798
	$U2_1$	3.41(2)	3.510(2)	3.5544
	$U1_1$	3.53(2)	3.622(2)	3.6712
	U2	3.634(9)	3.564(2)	3.5673
	$U2_1$	3.65(2)	3.663(2)	3.6237
	U2	3.67(2)	3.753(2)	3.7724
	$U2_1$	3.68(2)	3.833(2)	3.8724
	$U1_1$	3.74(1)	3.622(2)	3.6716
	$U1_1$	3.77(2)	3.873(2)	3.8396
	U2	3.83(2)	3.893(2)	3.8967
$U1_1$	$Ir1_1$	2.80(1)	2.805	2.792
	Ir2	2.83(2)	2.861	2.848
	Ir1	2.84(2)	2.841	2.827
	Ir2	2.85(2)	2.872	2.864
	Ir1	2.87(2)	2.853	2.846
	$Ir1_1$	2.92(2)	2.959	2.980
	$Ir2_1$	3.01(1)	3.003	3.062
	$U2_1$	3.49(2)	3.510	3.554
	U2	3.59(2)	3.564	3.567
	U2	3.67(2)	3.753	3.624
	$U2_1$	3.80(3)	3.833	3.772
U2	Ir2	2.80(1)	2.824(2)	2.808
	$Ir1_1$	2.85(1)	2.862(2)	2.839
	$Ir2_1$	2.85(1)	2.831(2)	2.808
	$Ir1_1$	2.86(1)	2.865(2)	2.872
	$Ir2_1$	2.87(2)	2.848(2)	2.847
	Ir1	3.018(8)	3.158(1)	3.189
	Ir2	3.036(8)	3.253(2)	3.273
	$U2_1$	3.51(2)	3.399(2)	3.319
	$U2_1$	3.59(2)	3.665(2)	3.728
	$U2_1$	3.84(2)	3.665(2)	3.728
$U2_2$	Ir1	2.80(3)	2.862	2.839
	Ir2	2.83(3)	2.824	2.808
	$Ir2_1$	2.82(2)	2.831	2.808
	Ir1	2.86(3)	2.865	2.872
	Ir2	2.87(3)	2.848	2.847
	$Ir1_1$	3.14(2)	3.158	3.189
	$Ir2_1$	3.28(2)	3.253	3.273
Ir1	$Ir2_1$	2.89(1)	2.953(2)	3.053
	$Ir1_1$	2.97(1)	2.981(2)	3.070
	Ir2	3.41(2)	3.221(2)	3.239
$Ir1_1$	Ir2	2.98(1)	2.953	3.053
	$Ir2_1$	3.173(8)	3.221	3.239
Ir2	$Ir2_1$	2.93(1)	2.908(2)	2.990

Table S 5: Atomic displacement parameters of UIr from single crystal and powder X-ray diffraction at room temperature. All atoms occupy the position 4*e* with site symmetry 1.

Atom	U^{11} / pm^2	U^{22} / pm^2	U^{33} / pm^2	U^{12} / pm^2	U^{13} / pm^2	U^{23} / pm^2	U_{eq} / pm^2
Single crystal data							
U1	115(4)	88(3)	66(4)	0	10(2)	0	90(2)
U2	111(4)	108(3)	79(4)	0	14(2)	0	99(2)
Ir1	134(5)	94(3)	80(4)	0	31(3)	0	101(2)
Ir2	123(4)	100(3)	94(4)	0	31(3)	0	104(2)
Powder data							
U1	132(18)	110(20)	132	0	0	0	127(12)
U2	132	110	132	0	0	0	127
Ir1	170(30)	60(30)	170	0	80(30)	0	127(16)
Ir2	170	60	170	0	80	0	127

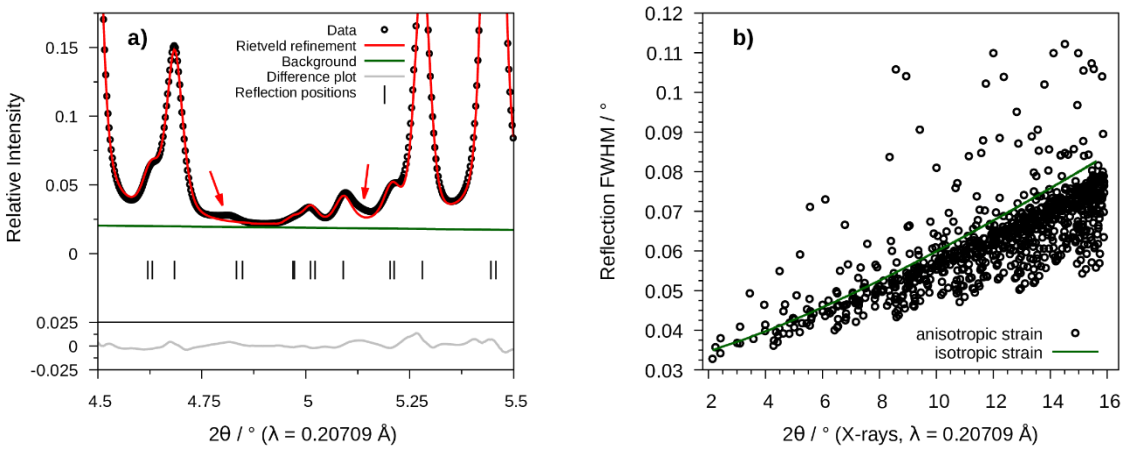

Figure S 3: Details of the Rietveld refinement of UIr. **a)** Section of the powder X-ray diffraction pattern highlighting reflections with pronounced asymmetric profiles with arrows. **b)** Comparison of the reflection FWHM of an isotropic particle strain model with the anisotropic particle strain model of Stephens.

S1.2 Magnetic and thermal characterization

S1.2.1 Experimental procedure

Thermal analysis of UIr was performed using powdered samples that were compacted to pellets with a hydrostatic press. Differential scanning calorimetry (DSC) measurements were done with a DSC-TGA 3 (Mettler Toledo) with a heating rate of 20 K·min^{-1} between room temperature and 1000 °C with argon as a sweeping gas. The measurements were performed in alumina crucibles. Differential thermoanalysis (DTA) experiments were performed using a Setaram Setsys 16/18 system equipped with a high-temperature DSC1600 measurement head. The samples were investigated between 300 °C and 1600 °C with a heating rate of 5 K min^{-1}. The measurements were performed in alumina crucibles with a thoria protective layer to prevent a reaction of the melt with the crucible material.

Heat capacity and magnetic measurements were performed with a DynaCool system of LOT-Quantum Design. The isobaric heat capacity $C_p(T)$ was measured using the Quantum Design heat capacity option in the temperature range from 1.8 to 300 K. The powder pellets were attached to the heat capacity puck of the Dynacool system using Apiezon N grease for thermal coupling to the platform.

DC-magnetic data were collected with the aid of the Quantum Design VMS option. Temperature dependent magnetic data was recorded in the range from 1.8 to 300 K with an applied field of 1 T. Field dependent magnetic data was recorded at 3 K. A full hysteresis loop was measured at fields between −9 T and 9 T. The collected data were corrected with respect to the diamagnetic moment of the polypropylene sample holder.

S1.2.2 Results

We have characterized UIr by means of magnetic and thermal measurements on polycrystalline samples. The inverse magnetic susceptibility at a magnetic field of 1 T is given in Figure S 4a. UIr orders ferromagnetically below 50 K. We have derived a Curie temperature of 47 K from the temperature dependency of the magnetization shown in the inset of Figure S 4a that is in good agreement with literature data collected in Table S 6. The obtained spontaneous magnetization μ_s of 0.41 μ_B per uranium atom is somewhat in between the literature values derived from polycrystalline UIr. The susceptibility between 50 K and 400 K can be fitted by a modified Curie-Weiss law $\chi = C / (T - \theta_p) + \chi_0$ with the fitting constants C = 0.486(1) K cm³ mol^{-1}, θ_p = 48.8(1) K and χ_0 = 868(8) 10^{-6} cm³ mol^{-1}. The so derived effective magnetic moment of 1.63 μ_B is more than four times larger than the spontaneous magnetization reflecting the itinerant magnetism of ferromagnetic UIr.[1] The Curie-Weiss parameters are strongly dependent on the investigated temperature range. Our results are in good agreement with investigations from Dommann and coworkers[2] reporting an effective magnetic moment of 1.67 μ_B and a paramagnetic Curie temperature of 46 K between 50 K and 100 K as given in Table S 6. Their high-temperature data for T > 500 K yields a strongly negative paramagnetic Curie temperature and an effective magnetic moment of 3.6 μ_B which is almost the same as the $5f^2$ or $5f^3$ free ion values of 3.58 μ_B and 3.62 μ_B, respectively. This behavior is discussed as a temperature dependent change from itinerant to localized magnetism in UIr.[2,3]

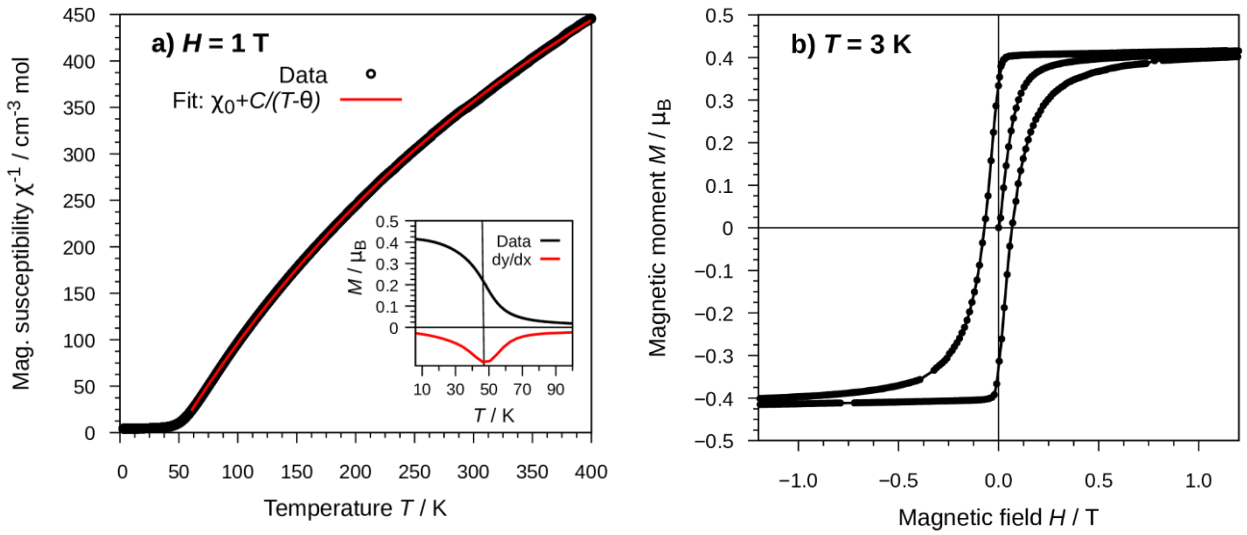

Figure S 4: Magnetic data of UIr. **a)** Inverse susceptibility of UIr at a magnetic field of 1 T (circles) and fit (red line) with a modified Curie-Weiss law ($\chi = C / (T - \theta_p) + \chi_0$) with the fitting constants C = 0.486(1) K cm³ mol^{-1}, θ_p = 48.8(1) K, χ_0 = 868(8) 10^{-6} cm³ mol^{-1}. The inset displays temperature dependency of the magnetization. The ferromagnetic transition at 47 K is derived by the first derivative (red line). **b)** Section of the hysteresis of UIr at a temperature of 3 K recorded with a field from −9 T to 9 T.

Table S 6: Magnetic properties of polycrystalline UIr in comparison to literature data: the spontaneous moment μ_s, the Curie temperature T_C, the effective moment μ_{eff}, the paramagnetic Curie temperature θ_p, and the temperature range ΔT used for the Curie-Weiss fit.

Reference	μ_s / μ_B per U atom	T_C / K	μ_{eff} / μ_B	θ_p / K	ΔT
This work	0.41	47	1.63	+48.8(1)	50 K to 400 K
[4]	0.31	44	2.91	-41	200 K to 300 K
[2]	0.48	46	1.67	+46	50 K to 100 K
			3.6	-430	> 500 K

Figure S 4b displays the magnetic hysteresis loop of polycrystalline UIr recorded at 3 K. It possesses similar characteristics as described in literature:[2] a nearly rectangular form with a remanent magnetization that equals the spontaneous magnetic moment and a small coercive field of about 0.07 T. We have performed thermal analysis of UIr to investigate a possible temperature driven phase transition that explain the observed twinning. Siegrist and coworkers had performed DTA experiments that excluded a phase transition below 530 K.[5] We have performed DSC as well as DTA experiments between room temperature and 1000 °C. However, we were not able to detect any phase transition within this temperature range as shown in Figure S 5a. Our DSC measurement setup is limited to 1000 °C and the DTA high-temperature measurement setup is not sensitive below 300 °C. We thus cannot sample the whole temperature range from the melting point of UIr to room temperature so that small heat effects may be overlooked that depend on the heating history.

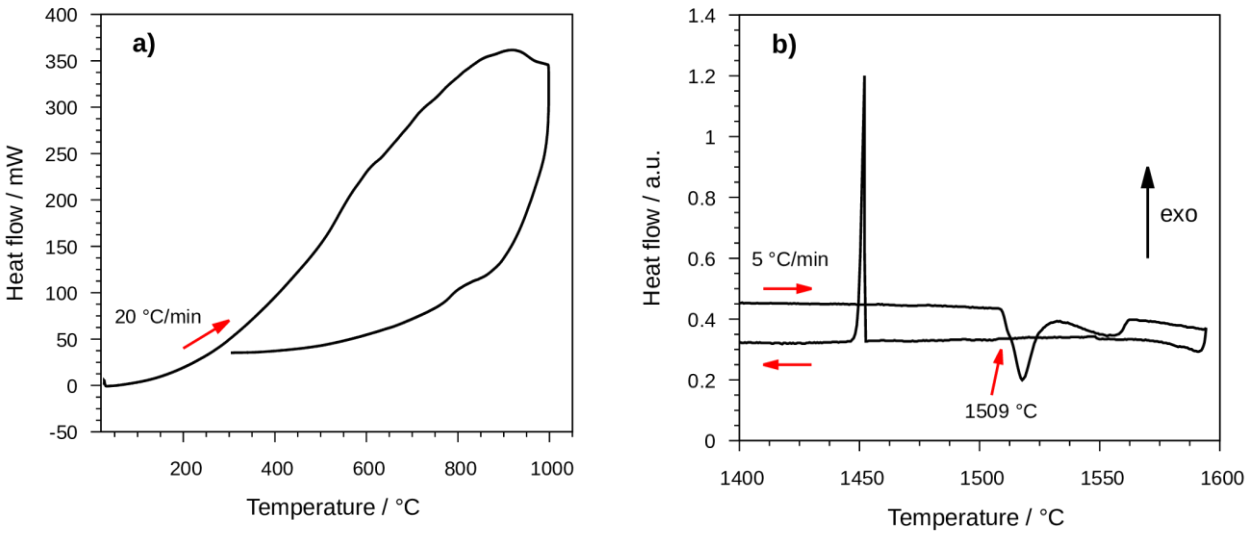

Figure S 5: Thermal analysis of UIr. **a)** DSC of UIr. The data was recorded between RT and 1000 °C with a heating rate of 20 °C per minute. **b)** DTA of UIr. The data was recorded between 300 °C and 1590 °C with a heating rate of 5 °C per minute.

Furthermore, we re-investigated the melting point of UIr by performing DTA of UIr between 300 °C and 1590 °C. Within this temperature range two endothermic signals in the heating curve and one exothermic in the cooling curve are found, that are shown in Figure S 5b. We have derived a melting point of 1509 °C of UIr from the first endothermic signal that is approximate 40 °C higher than the reported literature value from pyrometer measurements.[6] The solidification of UIr takes place with a pronounced hysteresis of about 60 °C and a strong and sharp exothermic signal at around 1450 °C. The nature of the second, broad endothermic signal at around 1550 °C cannot be assigned from our data with certainty. UIr is reported to melt congruently, so that only one endothermic signal is expected.[6] The position of its maximum varies from 1530 °C to 1580 °C and also its form it's not reproducible. It may result from a peritectic decomposition of UIr into UIr_2 ($Fd\bar{3}m$, $cF24$) and a uranium rich melt:

	$UIr_{(s)} \rightarrow UIr_{2(s)} + l$	(1)

UIr_2 is the adjacent phase of UIr in the binary phase diagram of uranium and iridium. We always find reflections of UIr_2 in the powder diffractograms from DTA experiments of UIr. However, as also UO_2 is always present in these samples, it is not possible to distinguish between the proposed peritectic reaction as given in Equation 1 and an oxidation of the melt itself:

	$2\ UIr_{(l)} + O_2 \rightarrow UIr_{2(s)} + UO_2$	(2)

It is therefore not possible from our experimental setup to determine the melting mechanism of UIr. Metallographic investigations may be necessary to resolve this issue.

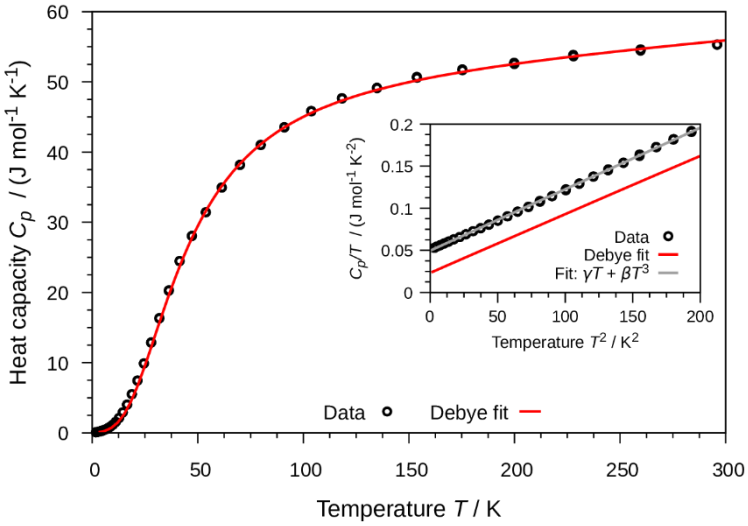

Figure S 6: Heat capacity of UIr between 1.8 K and 300 K. Data (circles) in comparison to a Debye model (red line). The inset displays the low temperature data in comparison to the Debye fit (red line) and a polynomial fit (grey line). Fit parameters are given in Table S7.

Furthermore, we have characterized UIr by means of heat capacity measurements between 300 K and 1.8 K as given in Figure S 6. The high-temperature data above the ferromagnetic transition at 47 K can be fitted with a Debye model with a Debye temperature θ_D of 179 K and a linear specific heat coefficient γ of 23(1) mJ/K^2 as shown by the red curve in Figure S 6. The fit parameters are given in Table S 7. The high-temperature fit cannot capture the experimental low temperature data as shown in the inset of Figure S 6. It can be described with a polynomial fit from 1.8 K to 15 K with a linear term γ accounting

for the electronic as well as the spin-wave specific heat and a cubic term β accounting for the phonon contributions.[4] The so derived value of γ is with 48(1) mJ/K^2 approximately twice as high as the obtained value from the high-temperature data that do not include the spin-wave contributions. However, our low-temperature experimental values of γ and θ_D derived from β are in good agreement with previous measurements reported in literature as summarized in Table S 7.

Table S 7: Heat capacity data of polycrystalline UIr in comparison to literature and spin-polarized DFT calculations. The DFT calculations are based on the CrB structure type. θ_D: the Debye temperature, γ: the linear specific heat coefficient.

Temperature range / Method	θ_D / K	γ / mJ K^{-2}	Reference
	174	48(1)	This work
0 – 15 K[a]	173	40	[4]
	181	46(1)	[7]
60 – 300 K[b]	179	23(1)	This work
DFT	177	20	This work

[a]Derived from fit: $C_p = \gamma T + \beta T^3$, $\beta = 12\pi^4\, n/5\, \theta_D^3$, *n*: atoms per f.u., [b]Derived from Debye model fit.

Table S 8: PAW Pseudopotential (PP) generation files for the *atomic* code of the *Quantum Espresso* distribution.

Scalar relativistic uranium PP	Fully relativistic uranium PP	Scalar relativistic neptunium PP
&input title = 'Uran' atom = 'U', dft = 'pbe', config = '[Rn] 5f3.0 6d1.0 7s2 7p0', rel = 1, iswitch = 3 / &inputp lpaw=.true. pseudotype=3, file_pseudopw='U.pbe-spn-kjpaw_MS.UPF', author='MSa', lloc = -2, rcloc = 1.4 nlcc = .true. new_core_ps=.true. rcore = 1.15, which_augfun='PSQ', rmatch_augfun = 1.4, rmatch_augfun_nc = .true., tm=.true., lgipaw_reconstruction=.true., use_paw_as_gipaw=.true., / 8 6S 1 0 2.00 0.00 1.30 1.75 0.0 7S 2 0 2.00 0.00 1.30 1.75 0.0 6P 2 1 6.00 0.00 1.40 2.00 0.0 7P 3 1 0.00 3.50 1.40 2.00 0.0 6D 3 2 1.00 0.00 1.30 2.20 0.0 6D 3 2 0.00 3.50 1.30 2.20 0.0 5F 4 3 3.00 0.00 1.30 1.80 0.0 5F 4 3 0.00 1.20 1.30 2.30 0.0	&input title = 'Uran' atom = 'U', dft = 'pbe', config = '[Rn] 5f3.0 6d1.0 7s1.9 7p0', rel = 2, nld = 8, dx = 0.008 iswitch = 3 / &inputp lpaw=.true. pseudotype=3, file_pseudopw='U.rel-pbe-spn-kjpaw_MS.UPF', author='MSa', lloc = -2, rcloc = 1.4 nlcc = .true. new_core_ps=.true. rcore = 1.15, which_augfun='PSQ', rmatch_augfun = 1.4, rmatch_augfun_nc = .true., tm=.true., lgipaw_reconstruction=.true., use_paw_as_gipaw=.true., / 9 6S 1 0 2.00 0.00 1.30 1.75 0.0 7S 2 0 1.90 0.00 1.30 1.75 0.0 6P 2 1 6.00 0.00 1.40 2.10 0.0 7P 3 1 0.00 0.50 1.40 2.10 0.5 7P 3 1 0.00 3.50 1.40 2.20 1.5 6D 3 2 1.00 0.00 1.30 2.20 0.0 6D 3 2 0.00 3.50 1.30 2.20 0.0 5F 4 3 3.00 0.00 1.30 1.80 0.0 5F 4 3 0.00 1.20 1.30 2.30 0.0	&input title = 'Neptunium' atom = 'Np', dft = 'pbe', config = '[Rn] 5f4.0 6d1.0 7s2.0 7p0', rel = 1, iswitch = 3 / &inputp lpaw=.true. pseudotype=3, file_pseudopw='Np.pbe-spn-kjpaw_MS.UPF', author='MSa', lloc = -2, rcloc = 1.3 nlcc = .true. new_core_ps=.true. rcore = 1.15, which_augfun='PSQ', rmatch_augfun = 1.40, rmatch_augfun_nc = .true., tm=.true., lgipaw_reconstruction=.true., use_paw_as_gipaw=.true., / 8 6S 1 0 2.00 0.00 1.30 1.60 0.0 7S 2 0 2.00 0.00 1.30 1.60 0.0 6P 2 1 6.00 0.00 1.40 2.00 0.0 7P 3 1 0.00 3.50 1.40 2.00 0.0 6D 3 2 1.00 0.00 1.40 2.20 0.0 6D 3 2 0.00 2.50 1.40 2.20 0.0 5F 4 3 4.00 0.00 1.40 1.80 0.0 5F 4 3 0.00 0.50 1.40 2.30 0.0

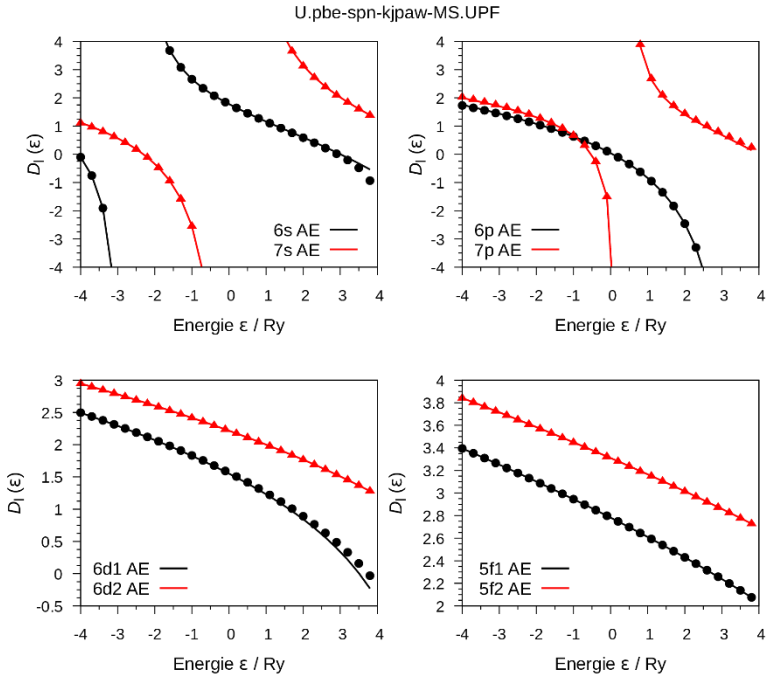

Figure S 7: The logarithmic derivatives $D_l(\varepsilon) = \frac{d}{dr}\ln R_l(r,\varepsilon)\Big|_{r=r_0}$ of the scalar-relativistic uranium PAW-PP. Symbols: PP results. Lines: all-electron results. In case of the d and f angular momentum channel the numbers refer to the two projector functions used for each channel.

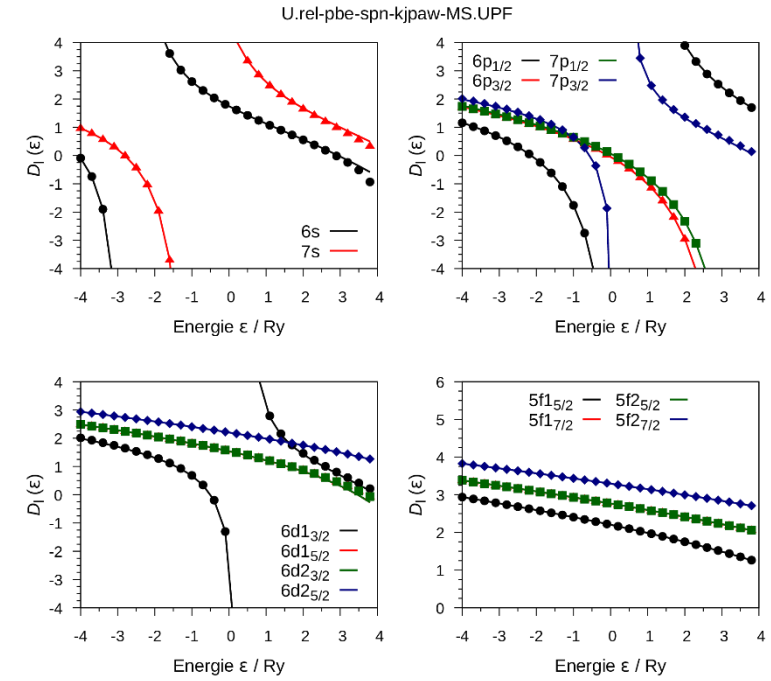

Figure S 8: The logarithmic derivatives $D_l(\varepsilon) = \frac{d}{dr}\ln R_l(r,\varepsilon)\Big|_{r=r_0}$ of the fully-relativistic uranium PAW-PP. Symbols: PP results. Lines: all-electron results. In case of the d and f angular momentum channel the numbers refer to the two projector functions used for each channel.

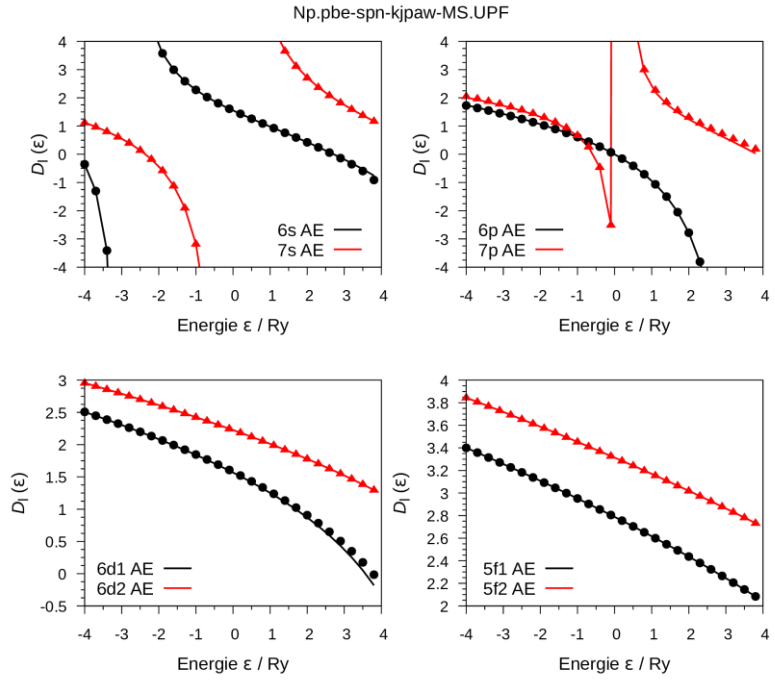

Figure S 9: The logarithmic derivatives $D_l(\varepsilon) = \frac{d}{dr} \ln R_l(r,\varepsilon)\Big|_{r=r_0}$ of the scalar-relativistic neptunium PAW-PP. Symbols: PP results. Lines: all-electron results. In case of the d and f angular momentum channel the numbers refer to the two projector functions used for each channel.

Table S 9: PBE total energy differences (ΔE) and $5f$ eigenvalue differences ($\Delta\varepsilon_{5f}$) of the generated scalar relativistic PAW-PP's of uranium and neptunium with respect to all-electron results for different atomic test configurations.

Element	Test configuration	$\Delta\varepsilon_{5f}$ / mRy	ΔE / mRy
Uranium	$5f^3\,6d^1\,7s^2$	0.03	0.00
	$5f^3\,6d^1\,7s^1$	0.11	0.28
	$5f^3\,6d^1\,7s^0$	0.18	0.71
	$5f^3\,6d^0\,7s^0$	0.39	1.13
Neptunium	$5f^4\,6d^1\,7s^2$	0.03	0.00
	$5f^4\,6d^1\,7s^1$	0.14	0.28
	$5f^4\,6d^1\,7s^0$	0.32	0.73
	$5f^4\,6d^0\,7s^0$	0.90	1.20

Table S 10: PBE total energy differences (ΔE) and $5f$ eigenvalue differences ($\Delta\varepsilon_{5f}$) of the generated relativistic PAW-PP of uranium with respect to all-electron results for different atomic test configurations.

Element	Test configuration	$\Delta\varepsilon_{5f7/2}$ / mRy	$\Delta\varepsilon_{5f5/2}$ / mRy	ΔE / mRy
Uranium	$5f^3\,6d^1\,7s^2$	0.02	0.01	0.00
	$5f^3\,6d^1\,7s^1$	0.07	0.08	0.00
	$5f^3\,6d^1\,7s^0$	0.17	0.17	0.00
	$5f^3\,6d^0\,7s^0$	0.32	0.34	0.01

Table S 11: Benchmark calculations of the scalar relativistic uranium and neptunium PAW-PP. Comparison between PBE/PAW and all-electron full-potential linearized augmented plane wave (FP-LAPW) calculations of lattice parameters and bulk moduli of selected compounds. All calculations are performed without spin-polarization.

Compound	Atomic volume V / a.u.³		Bulk modulus *B* / GPa	
	PAW-PP	FP-LAPW	PAW-PP	FP-LAPW
bcc-U	137	138	130	131
fcc-U	146	148	118	118
bcc-Np	119	122	171	168
fcc-Np	129	131	137	141

Table S 12: Optimized structural parameters of the *AB* compounds UIr, UPt, NpPt, and PdBi from spin-polarized DFT in the CrB structure type (*Cmcm*, *oC*8).

	Compounds			
	UIr	UPt	NpIr	PdBi
Lattice parameters				
a / Å	3.84831458	4.03485682	3.83833815	3.6479496262
b / Å	10.7848953	10.4012206	10.6070760	10.747356963
c / Å	4.02882609	4.24867267	4.11314360	4.5007334839
Structural parameters				
x(*A*1)	0	0	0	0
y(*A*1)	0.8645135242	0.870379210	0.8651093999	0.8590898211
z(*A*1)	¼	¼	¼	¼
x(*B*1)	0	0	0	0
y(*B*1)	0.6021113895	0.601342523	0.5996495298	0.5839548340
z(*B*1)	¼	¼	¼	¼

Table S 13: Optimized structural parameters from PdBi type ($P2_1/c$, *mP*16) *AB* compounds UIr, UPt, NpPt and PdBi from spin-polarized DFT:

	Compound *AB*			
	UIr	UPt	NpIr	PdBi
Lattice parameters				
a / Å	5.61877327	5.78078909	5.63680410	5.752713877
b / Å	10.6311812	10.6755526	10.5167294	10.87763711
c / Å	5.59739358	5.82234960	5.65393763	5.716168861
β / °	98.8163725	100.931153	99.9037939	79.23449053
Structural parameters				
x(*A*1)	0.1373314099	0.144065907	0.1386030981	0.3532377402
y(*A*1)	0.8617603137	0.859219113	0.8619785656	0.3559405613
z(*A*1)	0.8475208229	0.846779716	0.8493731944	0.8531316708
x(*A*2)	0.6060909349	0.614330167	0.6135186588	0.8848487268
y(*A*2)	0.8658165789	0.869162436	0.8666315722	0.3607026190
z(*A*2)	0.4074209959	0.403438980	0.4069812426	0.4070217735
x(*B*1)	0.0992424212	0.100194710	0.1032263577	0.8340667998
y(*B*1)	0.5998744658	0.593747808	0.5973920990	0.4113380561
z(*B*1)	0.8433463594	0.837928206	0.8428943263	0.9258047212
x(*B*2)	0.6454416365	0.650414959	0.6475711490	0.4038326865
y(*B*2)	0.6024894414	0.600703515	0.6004886054	0.4184376399
z(*B*2)	0.4099178293	0.409117923	0.4116317713	0.3382366874

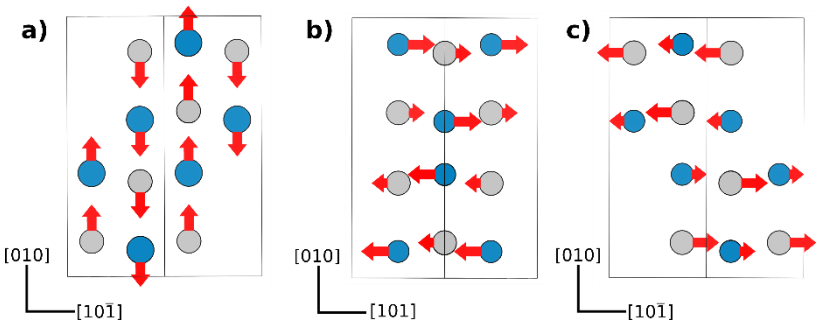

Figure S 10: The secondary distortion modes of UIr. The pictures display the CrB structure type (*Cmcm*, *oC*8) in the setting of the reference PdBi structure type ($P2_1/c$, *mP*16). Structure parameters are derived from spin-polarized DFT calculations. The directions of the atomic displacements correspond to the directions of the arrows. The lengths of the arrows have been exaggerated for a better visibility. **a)** The $\boldsymbol{\Gamma_1^+}$ distortion component viewed along the [101] direction (*a* axis in case of the *Cmcm* setting). **b)** The $\boldsymbol{Y_2^+}$ distortion component viewing along the [10$\bar{\mathbf{1}}$] direction (*c* axis in case of the *Cmcm* setting). **c)** The $\boldsymbol{Y_3^+}$ distortion component viewing along the [101] direction.

References

(1) Mohn, P. *Magnetism in the Solid State: An Introduction*, Corrected 2nd printing.; Springer series in solid-state sciences; Springer: Berlin ; New York, 2006.

(2) Dommann, A.; Hulliger, F.; Siegrist, T.; Fischer, P. The Magnetic Structure of UIr. *J. Magn. Magn. Mater.* **1987**, *67* (3), 323–330. https://doi.org/10.1016/0304-8853(87)90191-0.

(3) Galatanu, A.; Haga, Y.; Yamamoto, E.; D. Matsuda, T.; Ikeda, S.; Ōnuki, Y. High Temperature Magnetic Properties of UIr Single Crystals. *J. Phys. Soc. Jpn.* **2004**, *73* (3), 766–767. https://doi.org/10.1143/JPSJ.73.766.

(4) Bauer, E. D.; Freeman, E. J.; Sirvent, C.; Maple, M. B. High-Pressure Study of Ferromagnetic U $_x$ M $_{1-x}$ (M = Pt, Ir) Compounds. *J. Phys.: Condens. Matter* **2001**, *13* (24), 5675–5690. https://doi.org/10.1088/0953-8984/13/24/312.

(5) Siegrist, T.; Le Page, Y.; Gramlich, V.; Petter, W.; Dommann, A.; Hulliger, F. UIr, a PdBi-like Distorted CrB-Type Structure. *J. Less-Common Met.* **1986**, *125*, 167–174. https://doi.org/10.1016/0022-5088(86)90091-3.

(6) Park, J. J.; Mullen, L. R. Reactions of Uranium and the Platinide Elements. III. The Uranium-Iridium System. *J. Res. Natl. Bur. Stand. A Phys. Chem.* **1968**, *72A* (1), 19. https://doi.org/10.6028/jres.072A.003.

(7) Sakarya, S.; Knafo, W.; H. van Dijk, N.; Huang, Y.; Prokes, K.; Meingast, C.; von Löhneysen, H. Characterization of the Weak Itinerant Ferromagnetic Order in Single-Crystalline UIr. *J. Phys. Soc. Jpn.* **2010**, *79* (1), 014702. https://doi.org/10.1143/JPSJ.79.014702.